Experimental Investigation of Supercritical Carbon Dioxide in Horizontal Microchannels with Non-Uniform Heat Flux Boundary Conditions

Saad A. Jajja[a], Kyle R. Zada[a], Brian M. Fronk[a,*]

[a]*School of Mechanical, Industrial and Manufacturing Engineering*
Oregon State University
Corvallis, OR 97331 USA

Abstract

Supercritical carbon dioxide (sCO$_2$) experiences a drastic change in its thermophysical properties near the thermodynamic critical point. A non-linear thermophysical property variation can influence the heat transfer behavior of sCO$_2$ which is not predicted well by conventional single phase heat transfer theory. This can become a major hindrance in the effective design of heat exchangers using sCO$_2$ as a heat transfer fluid and operating in the vicinity of the critical point.

Previous investigations of sCO$_2$ heating have been primarily focused on macroscale, circular and uniformly heated channels at relatively low heat fluxes. It is unclear if models and correlations developed from large circular tube data can be scaled down to the microscale, non-circular channels subject to non-uniform heating. The present study experimentally investigates the turbulent heat transfer performance of sCO$_2$ in a microchannel heat exchanger operating in a horizontal configuration with a single wall non-uniform heat flux boundary condition. The test section has five parallel channels with a 0.75 mm hydraulic diameter and an aspect ratio of 1. The channels are fabricated using computer numerical control machining and the test section sealed using a diffusion bonding approach.

Data analysis techniques which employ 2-D and 3-D heat transfer models of the experimental test section are developed to calculate the average heat transfer coefficients for a given set of experimental conditions. Data are obtained over a wide range of experimental parameters including test section applied heat flux ($20 \leq q^{''} \leq 40$ W cm^{-2}), mass flux ($500 \leq G \leq 1000$ kg m^{-2} s^{-1}), reduced pressure ($1.03 \leq P_R \leq 1.1$), and inlet temperatures ($16 \leq T_{in} \leq 50$ ℃). The heat transfer data were screened for the presence of buoyancy and flow acceleration effects and then compared against correlations developed for turbulent subcritical and supercritical fluid flows.

Keywords: Microchannel, Heat transfer, Supercritical, Carbon Dioxide, Experimental, Non-Uniform Heat Flux, Buoyancy, Flow Acceleration

---

*Corresponding author
  Email address: `brian.fronk@oregonstate.edu` (Brian M. Fronk)

1. Introduction and Prior Work

Microchannel based heat exchangers using supercritical carbon dioxide (sCO_2) as a heat transfer fluid are poised to become integral components of the next generation of highly efficient energy systems. Potential applications include the receivers for concentrated solar power tower systems [1]–[3], printed circuit board heat exchangers (PCHE) for the recuperators in the supercritical Brayton cycles [4] and thermal management of high heat generating electronics [5]. In the case of solar thermal and electronics cooling applications, sCO_2 may be subjected to non-uniform heating boundary conditions. Before any attempt is made to design these heat exchangers, heat transfer models that account for the non-linear variations in the thermophysical properties of sCO_2 in the proximity of the thermodynamic critical point are required. This is especially true for thermal management applications where the desired operating conditions will span the critical point.

Near the critical point, the specific heat capacity and Prandtl numbers exhibit a sharp peak as shown in Figure 1(a). The temperature at which the peak occurs for a given
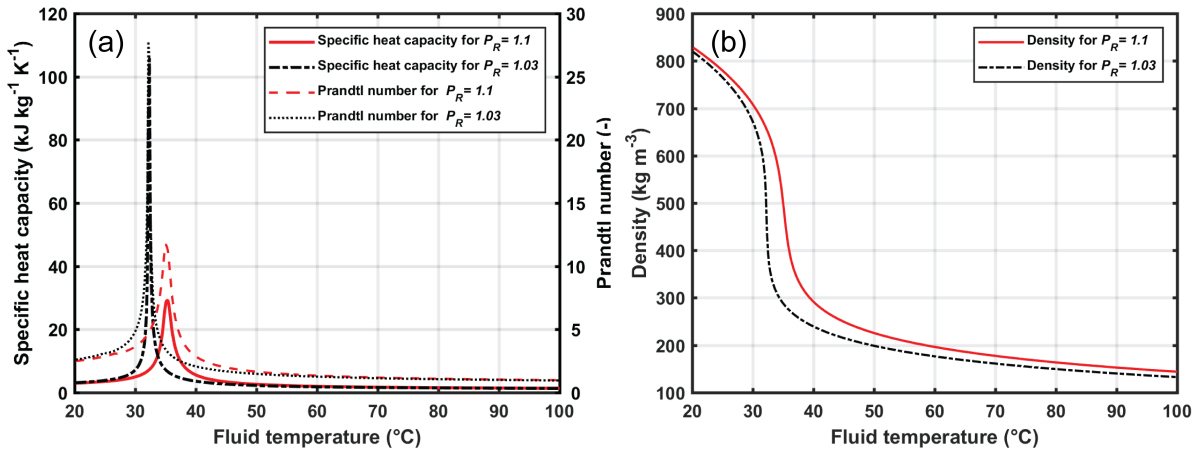

Figure 1: Variation of properties with temperature for CO_2 at two reduced pressures.(a) Specific heat capacity and Prandtl number. (b) Density

pressure is referred to as the pseudo-critical temperature. As the pressure increases, the magnitude of the peak decreases and the pseudo-critical temperature increases. Figure 1(b) shows a steep decrease in density near the pseudo-critical point, resulting in a transition from "liquid-like" to "vapor-like" properties without formation of separate liquid or vapor phases. For turbulent flows in heated channels, enhancement in heat transfer is expected in the proximity of the pseudo-critical point as a consequence of a large increase in the Prandtl number. However, the exact magnitude of this enhancement would be affected by the influence of both axial and radial/transverse density gradients in the flow channel.

Transverse/Radial gradients in the fluid density will induce buoyancy forces in the flow cross section, which depending upon the orientation of the test section can either enhance or suppress the turbulent thermal transport. For upward flows in vertical tubes, buoyancy forces initially act to suppress the turbulent thermal transport but as the relative magnitude

of the buoyancy forces increases, a recovery in the heat transfer is observed [6]–[8]. How-ever, for downward flows in vertical channels, buoyancy forces impose an adverse pressure gradient on the turbulent boundary layer which leads to an increased rate of turbulence production and hence an enhancement in the heat transfer is observed [6], [7]. It is also very likely that under heating conditions, axial variations in the density will impose a favorable pressure gradient on the turbulent boundary layer which will lead to the thickening of the viscous sub-layer and a suppression of turbulent transport quantities [9]. If the favorable pressure gradient is strong enough, the entire turbulent boundary layer can undergo a reverse transition to a laminar boundary layer which is referred to as *re-laminarization*.

In the following paragraphs, results and insights from different studies will be summa-rized that investigated the influence of buoyancy and flow acceleration on the heat transfer performance of sCO$_2$. Attention will be paid to studies in which the test sections operated in a horizontal orientation and the need for the present investigation will be established.

For horizontal flow configuration, buoyancy force, depending upon the heat flux boundary conditions, can cause stable or unstable stratification in the flow channel. Studies on the structures of stably stratified boundary layer flows point to the suppression of turbulent flow fluctuations as a consequence of buoyancy forces [10]. This is explained by the fact that part of the turbulent kinetic energy is dissipated in overcoming the buoyancy forces. However, for unstable thermally stratified flow in channels, the additional mixing induced by buoyancy forces, can act to enhance the heat transfer. The magnitude of this enhancement will ultimately depend on the applied heat flux boundary conditions and the mass flux of the sCO$_2$ in the flow channel.

Adebiyi and Hall [11] experimentally investigated the heat transfer performance of sCO$_2$ in a horizontal pipe (ID of 22.14 mm) with uniformly applied heat flux. The Reynolds numbers ranged from 2×10^4 to 2×10^5. For their experimental investigations, circumferential variations of the wall temperature were observed, with deterioration in heat transfer (higher wall temperatures) at the top surface of the tube. This phenomenon was attributed to the presence of buoyancy forces in the flow cross section, which led to an accumulation of low-density, lower conductivity fluid at the top of the flow channel. Similar variations in the circumferential wall temperatures for supercritical flows in horizontal channels were reported by Pidaparti *et al.* [12] and Bazargan *et al.* [13].

To gain further insights into the exact mechanisms responsible for buoyancy influenced heat transfer in horizontal tubes, a computational study based on the experimental investi-gation of Adebiyi and Hall [11] was conducted by Wang *et al.* [14]. The authors quantified the magnitude of the buoyancy forces in the flow cross section by determining the Richard-son number which increased as the applied heat flux increased. These buoyancy forces were responsible for inducing secondary flow patterns in the channel cross section, which led to an accumulation of low density and low momentum fluid at the channel top surface. At the same time, these secondary flow circulation patterns were also responsible for increasing the velocity of the fluid near the bottom wall of the channel. Consequently, the turbulence intensity levels and the heat transfer were reduced at the top channel wall and enhanced at the bottom walls. This explains the circumferential variations in the wall temperatures for buoyancy influenced flows in horizontal flow geometries.

The bulk of studies in the open literature focus on the heat transfer performance of sCO_2 in macroscale flow geometries. Although, these studies provide important insights into the heat transfer phenomenon in the vicinity of the critical point, it is not clear if the insights from larger tubes can be extrapolated to the heat transfer behavior of sCO_2 in microscale ($D_H < 1$ mm) flow geometries. This is especially true for buoyancy forces, which are usually quantified by the Grashof Number (Gr) as shown in equation 1. As the hydraulic diameter decreases, the definition of the Grashof number suggests that the buoyancy forces will decrease along with their effects on heat transfer. However, for microchannel heat exchangers operating in the vicinity of the critical point and subjected to very high heat fluxes, substantial density gradients might be present in the flow field which can negate the reduction in the Grashof number as a result of a decrease in the hydraulic diameter. Therefore, there exists a need for experimental investigations that can elucidate the importance of buoyancy in microcscale heat exchangers.

$$Gr = \frac{g\beta(T_w - T_b)D_H^3}{\nu_b^2} \tag{1}$$

In recent years, a number of studies[15]–[18], investigated the heat transfer performance of sCO_2 in microscale flow geometries under cooling conditions for horizontal flow configurations. The experimentally determined heat transfer coefficients far from the pseudo-critical point were predicted with a reasonable accuracy (within 20 %) by conventional single phase turbulent flow correlations [15]. However, these correlations failed to capture the trends in the heat transfer coefficients in the vicinity of the pseudo-critical point. To better account for variable thermophysical property heat transfer in semi-circular microchannel flow channels under cooling conditions, a new heat transfer correlation was proposed [16]. This new correlation proposed by Kruizenga *et al.* [16] was based on the fact that buoyancy was not influencing their heat transfer data. The heat transfer data was screened for potential buoyancy effects using a criterion proposed by Petukhov and Polyakov [19]. It is also important to realize that a cooling boundary condition would result in high density fluid near the wall which is not the case for a heating boundary condition. Therefore, correlations developed for cooling of supercritical carbon dioxide might not be applicable under heating conditions.

One of few experimental studies which addresses the heat transfer performance of sCO_2 in microscale geometries under heating conditions was conducted by Liao and Zhao [20]. Stainless steel (AISI 304) miniature tubes of internal diameters ranging from 0.7 mm to 2.16 mm were tested under vertical and horizontal flow orientations. Supercritical CO_2 mass flow rates were varied from 0.02 to 0.2 kg min^{-1} and the applied heat flux ranged from 10^4 to 2×10^5 W m^{-2}. Heat transfer data was screened for the presence of buoyancy effects in both vertical and horizontal flow orientations. For horizontal flows, the ratio, $\frac{Gr}{Re^2}$ was evaluated and if this ratio was less than 10^{-3}, then the magnitude of buoyancy forces in the flow field could be considered negligible. After screening the data for buoyancy effects, the experimentally determined Nusselt numbers were compared against those predicted by the Dittus-Boelter correlation which is only applicable for single-phase pure forced convective heat transfer conditions. It was surprising to see that the experimental test cases liable to be influenced by buoyancy were predicted reasonably well by the Dittus-Boelter correlation.

This was especially true for the tube with an ID of 2.16 mm. However, for the tube with an ID of 0.7 mm, using the above mentioned buoyancy screening criterion, it was concluded that buoyancy effects are negligible. This should translate to a better agreement with the Dittus-Boelter correlation, however, this particular geometry had the worst agreement with the predictions of the Dittus-Boelter correlation. This was even true when the bulk fluid temperatures far exceeded the pseudo-critical temperature and any changes in thermophysical properties were minimal. The authors did not comment on this discrepancy but did end up proposing a heat transfer correlation for horizontal flows in microchannels which had a functional dependence on the ratio of the Grashof and Reynolds number squared. The observed behavior could be explained by the possible influence of flow acceleration on the heat transfer but the authors did not report a screening of their experimental data for potential flow acceleration effects.

The phenomenon of *re-laminarization* of the turbulent boundary layer as a consequence of bulk flow acceleration will always lead to a reduction in the heat transfer from the wall to the bulk of the flow. Unlike the effects of buoyancy forces, which depend on the orientation of the test section, flow acceleration can occur under any arrangement of the test section provided that the wall heat flux is strong enough to cause a significant change in the axial bulk fluid density. To account for these effects, a criterion that establishes a threshold below which the effects of flow acceleration on heat transfer can be ignored is required. J.D.Jackson developed a heat transfer correlation which accounted for the effects of flow acceleration on the heat transfer performance of fluids with significant property variations [21]. In the process of the development of this correlation, a threshold criterion was also proposed that quantified the thermally induced acceleration of the bulk fluid flow. Additionally, McEligot and Jackson [22] developed a similar criteria for non-circular ducts.

With the push towards the use of microscale geometries for the design of next generation of heat exchangers, it is not clear if the correlations proposed for macroscale, circular and uniformly heated channels at relatively low heat flux can be used for microscale, non-circular channels subject to non-uniform heating. This serves as a major motivation for the present study. The experimental investigation presented here focuses on developing experimental methods and data reduction approach to characterize the turbulent heat transfer performance of sCO_2 in a microchannel heat exchanger test section with low experimental uncertainty ($< \pm 15\%$). Experiments are conducted in a horizontal configuration with a non-uniform applied heat flux boundary condition. The experimental variables for this study include the test section applied heat flux ($20 \leq q'' \leq 40$ W cm^{-2}), mass flux ($500 \leq G \leq 1000$ kg m^{-2} s^{-1}), reduced pressure ($1.03 \leq P_R \leq 1.1$), and inlet temperatures ($16 \leq T_{in} \leq 50$ ºC).

2. Experimental Approach

2.1. Experimental Loop

A schematic of the supercritical heat transfer facility is shown in Figure 2. The sCO_2 loop operates at a single pressure and consists of four primary components: pre-heater, test section, post-cooler, and gear pump. The coolant loop consists of a 5 kW air-coupled chiller with a circulation pump. The facility was designed to ensure compatibility with carbon

dioxide at high pressures (up to $\simeq$ 18 MPa) and temperatures (up to 200°C). All rigid wetted components were constructed with stainless steel (304 or 316/316L) while all soft wetted components (seals, valve seats, etc.) were sealed with commercial grade Teflon or EPDM (Ethylene Propylene Diene Monomer).
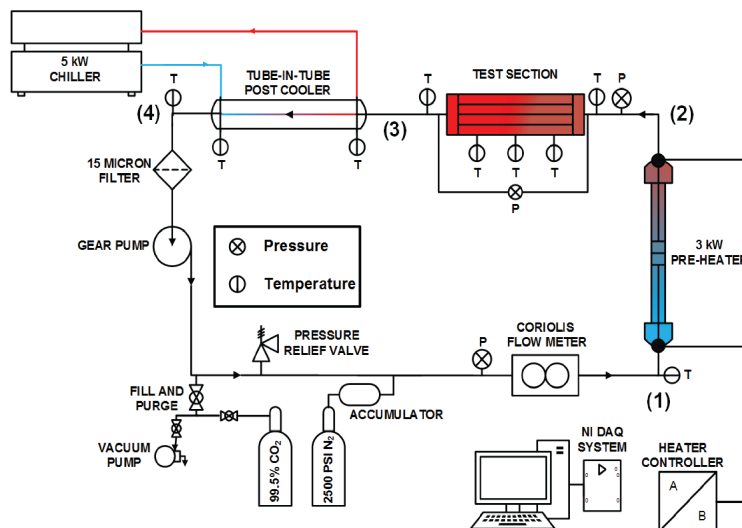

Figure 2: Schematic of experimental facility

During operation, the entire system is maintained at a pressure above the critical point, using a 0.95 L piston accumulator connected to a 17.5 MPa N_2 tank and a high-pressure regulator. At different points through the system, the fluid may be dense "liquid-like" fluid or low-density "vapor-like" fluid depending on the temperature. At state point 1 in Figure 2, dense "liquid-like" sCO_2 enters the annulus of a concentric tube pre-heating section. The sCO_2 exit temperature (test section inlet temperature) is adjusted to a specified value using SCR (PAYNE Engineering) controlled 1.5 kW cartridge heater elements, which are isolated from the CO_2. The pre-heater assembly is insulated with high temperature silicone foam pipe insulation. At the exit of the pre-heating section, the fluid enters the microchannel test section at state 2, where it is heated at a constant pressure and the heat transfer coefficient is measured, discussed below. A 100 W cartridge heater is controlled via a Variac autotransformer to adjust the constant heat flux being applied to the bottom surface (single-side) of the test section. The test section is insulated with a combination of high temperature rigid ceramic insulation and high temperature fiberglass insulation to minimize heat loss.

The hot sCO_2 exiting from the test section is cooled to a dense "liquid-like" state through the center tube of a tube-in-tube counter-flow post-cooler heat exchanger, located at state 3. The post-cooler consists of two heat exchangers arranged in series to accommodate the experimental heat loads and is insulated with fiberglass pipe wrap. A chilled $50-50\%$ glycol-water mixture flows in the annulus of the heat exchanger and is cooled via a Neslab Merlin recirculation chiller (Model M150) with a cooling capacity of 5 kW and a temperature range of 5 to 35°C. Finally, the supercritical CO_2 exits the post-cooler assembly as a dense, "liquid-like" supercritical fluid and is pumped back to the pre-heating section using a magnetically

coupled Micropump gear pump (Model GC-M23).

The experimental facility is instrumented with a variety of different measurement devices that are used to monitor temperature, pressure, flow rate, and electrical heat input, with locations shown in Figure 2. All bulk fluid temperatures (state 1 through 4) are measured using ungrounded T-type thermocouples with a nominal uncertainty of ± 0.5 °C or 0.4%. Gauge pressure is measured at the exit of the gear pump using an OMEGA current output transducer (Model PX-309-3KGI) with a nominal uncertainty of $\pm 0.25\%$ FS and range of 0 to 20.7 MPa. Absolute sCO$_2$ pressure is measured at the inlet of the test section using the Rosemount (Model 3051 SMV) pressure tansducer with a range of 0 to 3600 PSI. The mass flow rate of supercritical fluid is measured using a Coriolis flow meter immediately after the pump with a current output, nominal uncertainty of 0.1% of reading, and range of 0 to 325 kg hr^{-1}. An Ohio Semitronics wattage meter transducer (Model GW5-103E) is used to monitor the power supplied to the test section cartridge heater with a nominal uncertainty of 0.2% of reading and range of 0 to 100 W.

The data from the transducers are acquired using a National Instruments compact data acquisition chassis (Model NI-cDAQ-9174) with National Instruments current and voltage input modules (Model NI-9205, NI-9211 and NI-9203) and a 16-channel thermocouple input module (Model NI-9214). A GUI was developed within LabVIEW to display data in real-time and monitor trends during the experiment.

During each experimental run, data using the above equipment and experimental loop are recorded under steady-state conditions for a given heat flux, mass flux, reduced pressure, and inlet temperature. The system is turned on in stages, starting with adjustments in system pressure, mass flow rate, inlet temperature, and applied heat flux in small increments until the desired experimental conditions are achieved. The steady-state of the system is verified by recording the inlet and outlet temperatures of the test section over a duration of five-minutes. If the pre and post interval temperatures are within ± 0.25°C (within thermocouple uncertainty), the system is considered steady state and the data are recorded at a rate of 2 Hz for a duration of 5 minutes. If however, the system is not able to keep the inlet and outlet temperatures within ± 0.25°C, even after adjusting the SCR controls, the data are recorded at a rate of 2 Hz for a duration of 10 minutes. This reduces the precision error of the data in post-processing.

2.2. Test Section Design and Analysis

In the present study, a microchannel test section was designed and fabricated to handle high temperature and pressure conditions (up to 18 MPa and 200°C), resist the effects of corrosion, and non-invasively measure average heat transfer coefficient, with a low design stage uncertainty (> 15%). The test section under consideration has five parallel, square channels with a hydraulic diameter of 0.75 mm, aspect ratio of 1, and a total channel length of 50 mm. To ensure the fluid is hydrodynamically developed at the entrance of the 20 mm heated region, there is a 40D (30 mm) adiabatic section upstream. A flux meter is used with three sets of thermocouples at three evenly spaced axial positions (5 mm streamwise) along the heated portion of the test section to calculate the heat flux and wall temperature of the microchannel. An exploded view of the test section is shown in Figure 3, illustrating

the location of the fluid inlet/exit, cartridge heater, flux meter, and development/heated length.
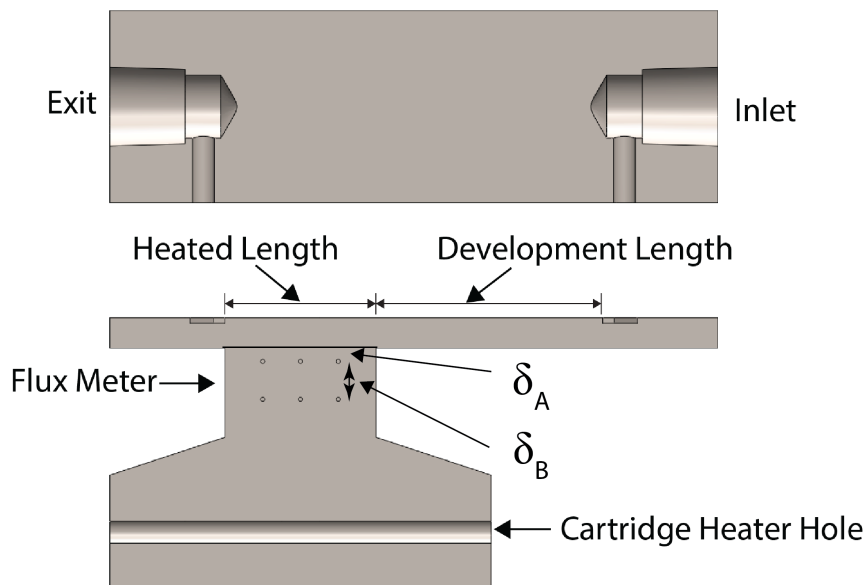

Figure 3: Cross-sectional view of microchannel test section CAD model.

The test section was fabricated from 316/316L dual certified stainless steel. The test section fabrication required a multi-step process involving both Computer Numerical Control (CNC) machining and diffusion bonding. First, the channel geometry and the inlet/exit plenum parts were machined. Next, the channel geometry was measured and verified using a ZeScope Optical Profiling System with a total uncertainty (repeatability, precision, and resolution) of $\pm 0.005 \mu m$. Multiple measurements at both the entrance and central region of the channels were used to determine an average channel height, width, and web thickness. The microchannel test section was then diffusion bonded in compliance of SAE-AMS-H-6875 Revision B. After the bonding process, the flux meter was machined out of the bottom portion of the test section. The final dimensions of the test section used in the current experiment can be found in Table 1 , showing the nominal, actual, and uncertainties for each of the critical dimensions.

To calculate the heat flux and wall temperature of the microchannel test section, K-type thermocouples (Model KMQSS-02U-6) with a nominal uncertainty of ± 1.1 °C or 0.4% were inserted in the locations indicated in Figure 3. Prior to fully insulating and conducting experiments the inlet, exit, and six flux meter thermocouples were calibrated against a temperature standard reference probe (P/N: FLUKE 5619) which had an uncertainty of ± 0.024ºC. In addition to the uncertainty associated with the thermocouples, the Analog to Digital Conversion (ADC) in the DAQ module can also introduce significant amount of uncertainty in the final measured value of the temperature. Therefore, the thermocouples were calibrated while they were connected to the DAQ module. A constant temperature bath which uses silicone oil (P/N: FLUKE 7109A) was used to conduct the calibrations for

8

Table 1: Microchannel test section dimensions with uncertainty

Type	Parallel (Square)		
Aspect Ratio (Width/Height)	1:1		
Number of Channels	5		
Development Length	30 mm		
	Nominal	Actual	Uncertainty
Channel Width	750 μm	750.02 μm	$\pm$5.53 μm
Channel Height	750 μm	737.32 μm	$\pm$6.16 μm
Web Thickness	1000.00 μm	991.85 μm	$\pm$7.90 μm
Channel Hydraulic Diameter	750 μm	743.62 μm	$\pm$4.15 μm
Flux Meter Length	20 mm	20.02 mm	$\pm$0.024 mm
Flux Meter Width	7.75 mm	7.75 mm	$\pm$0.024 mm
Flux Meter δ_A	5.00 mm	4.73 mm	$\pm$0.049 mm
Flux Meter δ_B	5.00 mm	5.00 mm	$\pm$0.025 mm

a temperature range of 10ºC to 140ºC . A calibration curve was generated which was used to post process the experimental results.

3. Data Analysis

3.1. Calculation of Heat Transfer Coefficient

Figure 4(a) shows a schematic of the side view of the test section and Figure 4(b) the top view of the microchannel flow passages inside this test section. To ensure a hermetic diffusion bond, a bonding region without flow channels was required, as shown in the Figure 4(b). The bonding region and the development length contribute to potential axial conduction and heat spreading at the junction of the flux meter and the main test section that must be accounted for in the data reduction. To address a similar problem of axial conduction in microchannel heat exchangers made of copper, Agarwal and Garimella [23] and Garimella *et al.*[24] developed a 2D resistance network model to do a segmental conjugate heat transfer analysis of their test section to calculate the refrigerant side heat transfer coefficients. A 2D approach by itself is not sufficient to capture the axial conduction and heat spreading phenomena expected here. Thus, in the present work, this approach is expanded by using a 3D finite element analysis coupled with a 2D resistance network model, which are solved in an iterative fashion, described below. A sample calculation is also presented to more clearly illustrate the approach.

First, the average heat flux through the flux meter is calculated using the experimental thermocouple measurements. Then, using this value as a constant heat flux boundary, a 3D conduction analysis of the test section in Figure 4 is conducted using COMSOL Multiphysics [25] to calculate a temperature distribution within the device. The fluid domain is not simulated, rather, a constant convection coefficient boundary is assumed in the fluid channels (Figure 4(b) with the average of the measured inlet/outlet sCO$_2$ temperatures used as the
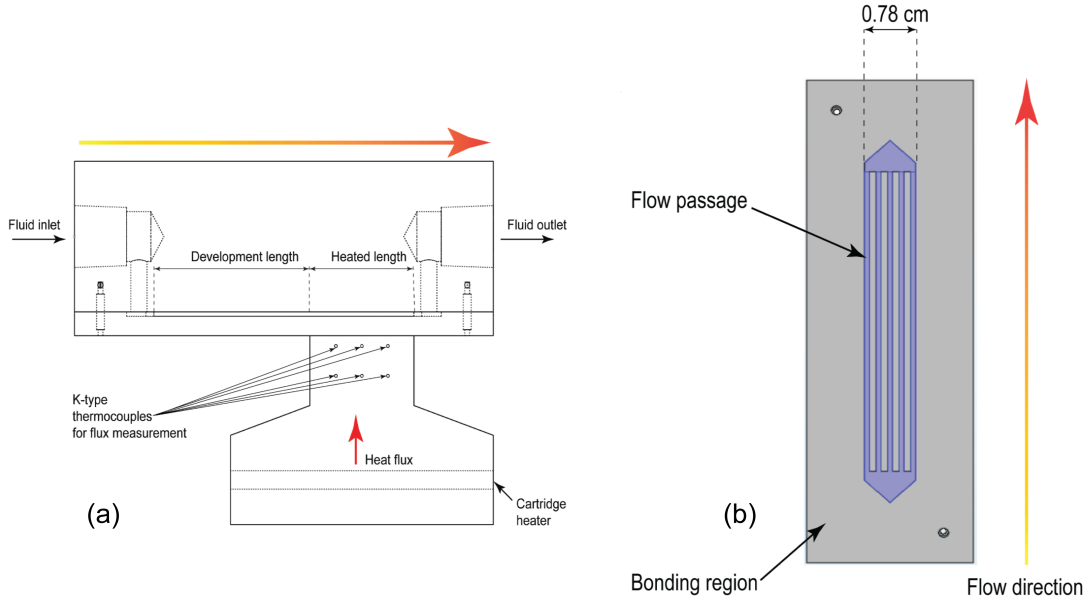
Figure 4: Schematic of the test section. (a) Side view (b) Top view of the flow channels

bulk temperature. Temperature dependent thermal conductivity of the test section material, AISI 316 stainless steel as predicted by Ho and Chu [26] was used in COMSOL. Physics controlled meshing option with extremely fine mesh size was used for this analysis. This mesh size was selected after doing a grid independence study which involved reducing the minimum mesh element size from 1.61E-5 m (extremely fine mesh option) to 1.61E-6 m, increasing the mesh elements from 191838 to 3892517 and solving for temperature profile of the test section. For both of these mesh sizes, the temperature solution at the flux meter thermocouple locations was identical which signifies that the temperature solution is no longer dependent on the size of the mesh elements.

For a given heat flux boundary condition, the value of the convective heat transfer coefficient was varied until the average of three temperatures at the top flux meter thermocouple locations Figure 4(a) was within ±0.22°C of the experimentally determined average at the same location. This particular tolerance results from considering the total experimental uncertainty of ±0.1°C resulting from using calibrated K-type thermocouples in the test section flux meter and an additional uncertainty associated with the precise location of the temperature measurement in the actual flux meter holes. This uncertainty was set to be twice the total experimental uncertainty, i.e. ±0.20°C. Taking the Root Sum Squares (RSS) of these two uncertainties results in a tolerance of ±0.22°C. In addition to the calculated average convective heat transfer coefficient, the COMSOL model predicts the wall temperature distribution, and the heat flux distribution throughout the device, accounting for axial conduction and heat spreading effects.

After completing an initial 3D simulation using the sCO$_2$ bulk temperature as a boundary condition in the fluid domain, a 2D resistance network model is used to produce a more
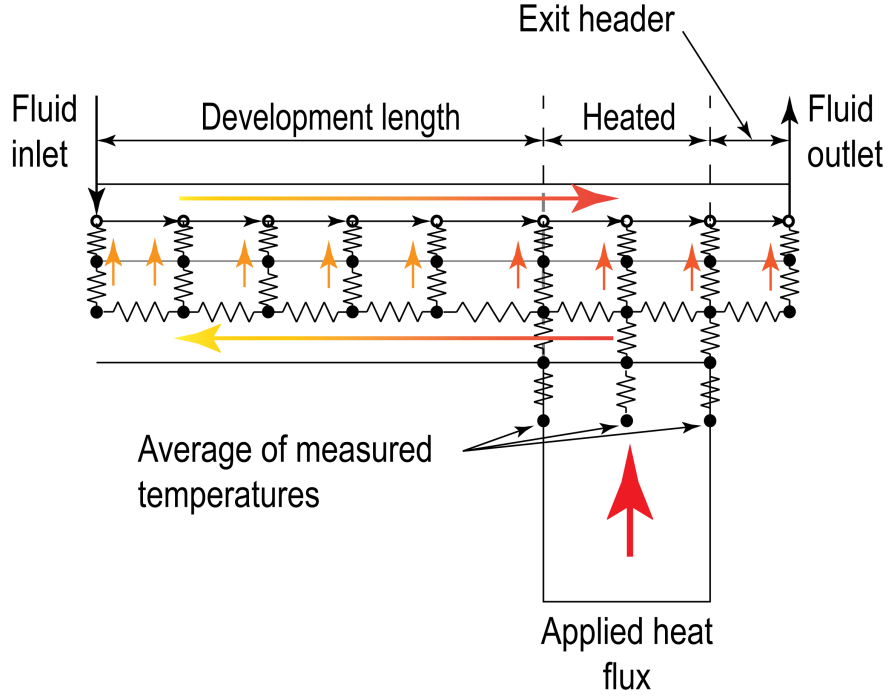
10

Figure 5: Resistance network model

realistic fluid temperature profile. As shown in Figure 5, the resistance network model is divided into three sections; the 30 mm unheated flow passage, 20 mm heated flow passage and the exit header. The open nodes in Figure 5(a) represent the fluid nodes while the filled black nodes represent the solid portion of the test section body. The inputs to this resistance network model are the measured heat flux (from flux meter thermocouples), fluid mass flow rate, absolute pressure and inlet temperature. Respective conductive and convective resistances are calculated based on the geometry of the test section. All the thermophysical properties of the fluid are evaluated at the test section absolute pressure and the temperature of the fluid nodes using the equation of state proposed by Span and Wagner [27]. A uniform convective heat transfer coefficient is assumed for all fluid segments. The values of the thermal conductivity of the test section are calculated using the thermal conductivity of AISI 316 stainless steel [26] at the average temperature of the nodes adjacent to each other. The model is solved by an iterative solution of the energy balance equations specified for each of the filled nodes and an overall energy balance on the model for closure. The resistance network model outputs are the fluid outlet temperature, the variation of the fluid temperature as a function of the flow length, the average heat transfer coefficient and the heat absorbed by the supercritical carbon dioxide in the unheated, heated and the exit header portions of the test section.

The calculated axial fluid temperature profile (rather than a fixed average bulk temperature) is then used in the 3D FEA model as a boundary condition with an unknown convective heat transfer coefficient in the microchannel array. The temperature distribution

11

Table 2: Measured inputs to the resistance network model

Input	Unit	Description	Value
T_{in}	°C	Inlet temperature of the fluid	20.45
$\dot{m}$	kg s^{-1}	Mass flow rate of the fluid	0.001377
P_{inlet}	kPa	Absolute pressure of the fluid	8111.46
$T_{FM,A,1}$	°C	1st flux meter thermocouple in top row	102.55
$T_{FM,B,1}$	°C	1st flux meter thermocouple in bottom row	169.78
$T_{FM,A,2}$	°C	2nd flux meter thermocouple in top row	100.94
$T_{FM,B,2}$	°C	2nd flux meter thermocouple in bottom row	164.56
$T_{FM,A,3}$	°C	3rd flux meter thermocouple in top row	96.61
$T_{FM,B,3}$	°C	3rd flux meter thermocouple in bottom row	161.33

is calculated in the solid domain only. Using the experimentally measured flux meter temperatures and applied heat flux, an iterative, inverse approach is again used to solve for the unknown heat transfer coefficient.

Finally, the convective coefficients predicted by COMSOL are used to calibrate the resistance network model. While the 2D model does consider axial conduction, it does not consider the 3D heat spreading from the flux meter into the bonded region. The calibration is based on the solution of the inverse model with the known heat transfer coefficient to determine an effective spreading thermal resistance in the 2D model. After this calibration, the average heat transfer coefficient predicted by the resistance network model is equal to that determined from the COMSOL simulations. This calibrated resistance network model is then used for the detailed uncertainty analysis using the Kline-McClintock [28] method of uncertainty propagation. This iterative 3D$\rightarrow 2D \rightarrow 3D \rightarrow$ 2D process is applied for each data point.

3.2. Sample Calculation

To better illustrate this data analysis approach, representative calculations for a data point at a reduced pressure of 1.1, heat flux of 20 W cm^{-2}, mass flux of 500 kg m^{-2} s^{-1} and an inlet temperature of 20°C are presented. The inputs to the resistance network model for this particular case are shown in Table 2. First, Fouriers law of heat conduction as represented by equation 2 is used to calculate the applied heat flux to the test section.

$$q''_{FM,ave} = -k_{FM,ave}\left(\frac{T_{FM,A,ave} - T_{FM,B,ave}}{\delta_B}\right) \qquad (2)$$

The average of the top three thermocouples ($T_{FM,A,ave}$) and the bottom three thermocouples ($T_{FM,B,ave}$) are calculated, and for this particular case are 100.03°C and 165.22°C, respectively. The thermal conductivity of the test section ($k_{FM,ave}$) is found as a function of the average temperature of all the flux meter temperatures, using the thermal conductivity of AISI 316 stainless steel [26], which is 15.25 W m^{-1} K^{-1}. The distance between the two rows (δ_B) of thermocouples is 5 mm, yielding a calculated average applied heat flux,

$(q''_{FM,ave})$ of 19.89 W cm^{-2}, or a total heat duty of 30.82 W applied to the test section. For this particular case, the model predicts that 24.5 W is transferred in the heated region while 2.98 W is transferred to the fluid in the exit header region and the remaining 3.64 W is conducted axially to the upstream development length. For this same case, COMSOL using the bulk fluid temperature predicts that 25.4 W ends up in the heated region, 2.4 W in the exit header and the remaining 3.20 W is conducted in the upstream unheated region. Since, these heat duties are within 5% of each other we can proceed with using the fluid temperature profile predicted by the resistance network model in COMSOL as an updated boundary condition. This fluid profile is shown in Figure 6(a) and is fitted by equation 3.
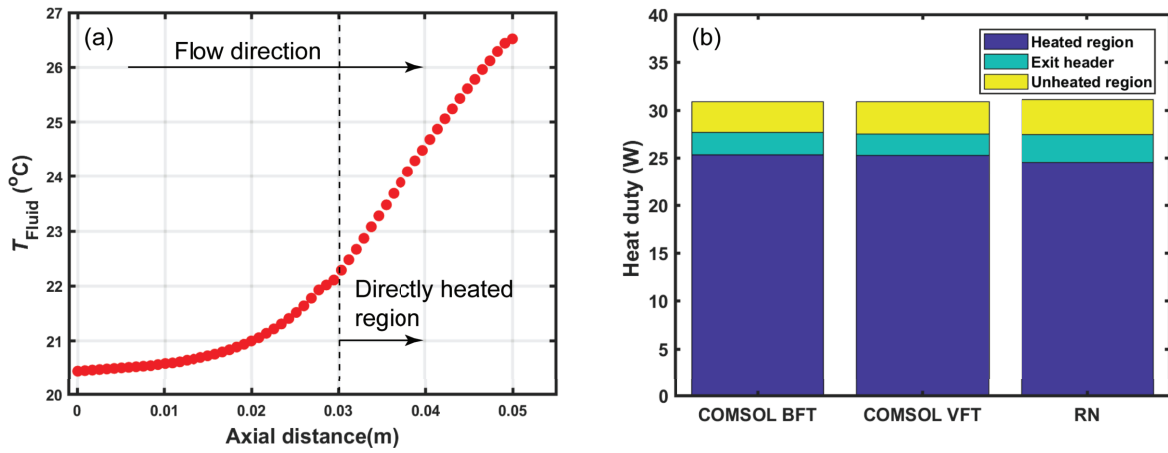
Figure 6: Sample calculation results for $P_R = 1.1$, $G = 500$ kg m^{-2}s^{-1}, $T_{in} = 20$°C and $q'' = 20$ W cm^{-2}.(a) Fluid temperature profile calculated by the resistance network model.(b) Comparison of heat duties for different portions of the test section calculated using the resistance network model and COMSOL Multiphysics

The heated length of the test section begins at the axial position of 0.03 m after which there is a significant increase in the fluid temperature.

$$T_{sCO_2} = -6.583 \times 10^7 x^5 + 3.371 \times 10^6 x^4 + 4.828 \times 10^4 x^3 - 269.9 x^2 - 12.01 x + 20.55 \quad (3)$$

Using this fluid temperature profile, the calculated average heat transfer coefficient using COMSOL is 3900 W m^{-2} K^{-1}. Figure 6(b) shows the comparison of heat duties for the three portions of the test section as predicted by COMSOL using both the variable fluid temperature profile (VFT) and the bulk fluid temperature (BFT) against those predicted by the resistance network (RN) model. For this particular case, COMSOL simulation predicts that about 5 W (16%) of the total heat duty is being conducted to the top test section cover and ends up heating the fluid from the top. In addition to the calculation of the average heat transfer coefficients, the average bottom, top wall and side wall temperatures of the flow passage are also extracted from the COMSOL simulation, which for this particular case are 32.78°C, 30.45°C and 31.58°C, respectively. These results indicate that the 3D data analysis approach is merited to provide the most accurate results.

13

3.3. Uncertainty Analysis

The four basic sources of uncertainty at the transducer level are the precision error, bias uncertainty, conversion of transducer output (e.g. current-to-voltage using shunt resistor circuit), and analog-to-digital conversion (ADC) using a data acquisition system. Using the Root-Sum-Squares (RSS) method, the different sources of uncertainty (e.g. 1, 2, 3) can be combined into a single overall uncertainty value (U_o) as shown in equation 4.

$$U_o = \sqrt{U_1^2 + U_2^2 + U_3^2 + ...} \tag{4}$$

Table 3: Measured variable uncertainty summary for sample case
$P_R = 1.1$, $G_{chan} = 1000$ kg m^{-2} s^{-1}, $q_{FM}'' = 20$ Wcm^{-2}, $T_{in} = 35.6$ °C

Variable	U_{Prec}	U_{bias}	$U_{bias,UTC}$	U_{ADC}	U_{tot}
$\dot{m}$(kg s^{-1})	$\pm 1.121 \times 10^{-5}$	$\pm 1.258 \times 10^{-6}$	$\pm 2.708 \times 10^{-5}$	$\pm 1.404 \times 10^{-4}$	$\pm 1.429 \times 10^{-4}$
P_{inlet} (kPa)	± 2.91	± 20.2	-	± 1.56	± 20.4
T_{in}(°C)	± 0.01	± 0.1	-	-	± 0.1
T_{ex}(°C)	± 0.01	± 0.1	-	-	± 0.1
$T_{FM,A,1}$(°C)	± 0.02	± 0.22	-	-	± 0.22
$T_{FM,B,1}$(°C)	± 0.02	± 0.22	-	-	± 0.22
$T_{FM,A,2}$(°C)	± 0.02	± 0.22	-	-	± 0.22
$T_{FM,B,2}$(°C)	± 0.02	± 0.22	-	-	± 0.22
$T_{FM,A,3}$(°C)	± 0.02	± 0.22	-	-	± 0.22
$T_{FM,B,3}$(°C)	± 0.02	± 0.22	-	-	± 0.22
Wattage (W)	± 0.04	± 0.17	± 0.20	-	± 0.26

Table 4: Uncertainty analysis summary for calculated quantities
$P_R = 1.1$, $G_{chan} = 1000$ kg m^{-2} s^{-1}, $q_{FM}'' = 20$ Wcm^{-2}, $T_{in} = 35.6$ °C

Variable	Unit	Value	U_{tot}	% uncertainty
D_H	μm	743.6	4.15	0.6
G_{chan}	kg m^{-2} s^{-1}	998.8	52.87	5.29
$q_{FM,ave}''$	Wcm^{-2}	19.81	0.11	0.5
$\dot{Q}_{tot}$	W	30.71	0.203	0.6
α_{sCO_2}	W m^{-2}K^{-1}	13000	1224	9.42

The total measurement uncertainty (at the transducer level) from an experiment is ultimately determined using the RSS method by incorporating the precision error and bias error. Sometimes a significant source of uncertainty is developed from the analog-to-digital conversion (ADC) of data into the data acquisition system. The ADC uncertainty for temperature measurements was eliminated by calibrating the thermocouples while they were attached to the DAQ module. The uncertainty in the measured variables for one of the test cases is summarized in Table 3. The uncertainties of the measured variables are then used to calculate uncertainties in the calculated parameters like the heat flux, mass flux, and the

14

heat transfer coefficient by using the using the Kline-McClintock method. The Engineering Equation Solver platform [29] was used to automate the process of uncertainty propagation and the results for the final uncertainties in the measured variables for one of the test cases are summarized in Table 4.

4. Results and Discussion

4.1. Experimental Results

The experiments in the present study explored the effects of mass flux ($500 \leq G \leq 1000$ kg m^{-2} s^{-1}), heat flux ($20 \leq q'' \leq 40$ W cm^{-2}), reduced pressure ($1.03 \leq P_R \leq 1.1$) and inlet temperatures ($16 \leq T_{in} \leq 50$ °C) on the heat transfer in parallel, square microchannel geometries with a hydraulic diameter of 0.75 mm and an aspect ratio of 1. A total of 70 data points were collected for the six different combinations of these experimental variables. For a given data set (e.g. one mass flux, one heat flux, and a range of inlet temperatures) the variation in inlet pressure, mass flux, and average heat flux was less than 1.5%, 6.2%, and 3.3%, respectively. The maximum uncertainty in the calculated average heat transfer coefficient is 10%. The maximum uncertainty for all the test cases occurs near the pseudo-critical temperature point, where the specific heat capacity spikes with a corresponding increase in the average heat transfer coefficient, which reduces the temperature differential between the wall and bulk fluid. Tabulated values of measured variables, calculated wall temperatures, calculated heat transfer coefficient and the calculated uncertainty in heat transfer coefficient are available in [30]

4.2. Test Section Heat Loss

To quantify the effects of heat loss from the test section during the experiments, the calculated thermal energy gained by the fluid ($\dot{Q}_{fluid}$) through the test section is compared to the power input to the cartridge heater ($\dot{Q}_{tot}$). The energy transferred to the fluid is determined by an energy balance where the inlet/exit enthalpies are determined from the measured temperatures at these locations and the inlet absolute pressure.

$$\dot{Q}_{fluid} = \dot{m}_{sCO_2} \times (h_{in} - h_{ex}) \tag{5}$$

$$R_Q = \frac{\dot{Q}_{fluid}}{\dot{Q}_{tot}} \tag{6}$$

The comparison of R_Q for a range of experimental conditions as a function of the ratio of bulk fluid temperature and the pseudo-critical temperature is shown in Figure 7 . For clarity, only the higher heat flux conditions (40 W cm^{-2}) are shown here as the test section temperature is higher which enhances the potential for heat loss from the test section. The highest uncertainty in R_Q occurs at the pseudo-critical point which stems from the small change in bulk fluid temperature due to the high heat capacity of the sCO$_2$. The heat losses from the test section for the majority of the data points are within 25% of the total power input to the cartridge heater. For the same applied heat flux, the increase in heat losses as we move away from the pseudo-critical point is explained by a decrease in the specific heat

15

capacity of the fluid coupled with higher bulk fluid temperatures. Combination of these factors raise the temperature of the test section body, which explains an increase in heat loss. In the data reduction, the actual heat duty supplied to the fluid is determined from the measured heat flux in the flux meter. As shown in Figure 3, the distance between the flux meter thermocouple location and the test section bottom wall is at maximum 10 mm. Thus, most of the heat loss from the heater occurs prior to the heat flux meter over the much larger surface area of the heater body.
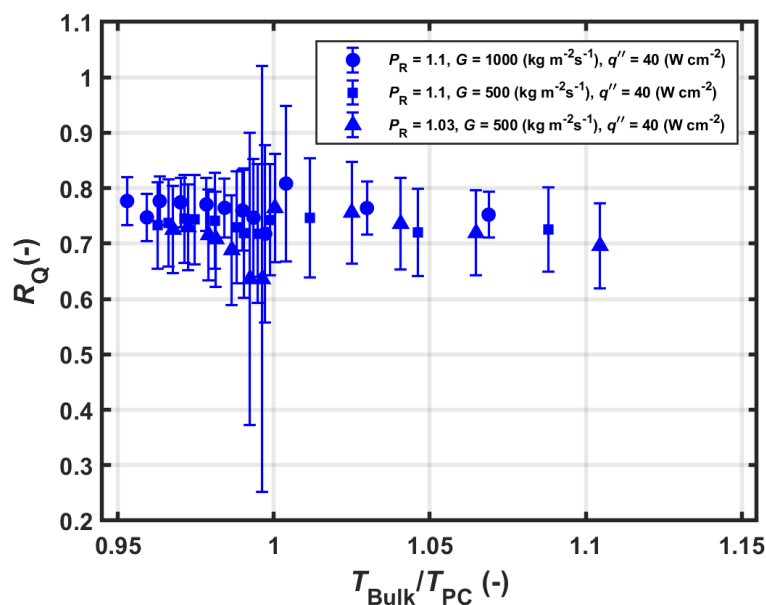
Figure 7: Heat input ratio as a function of the ratio of the bulk fluid temperature and the pseudo-critical temperature

4.3. Trends in Average Heat Transfer Coefficients

The average heat transfer coefficients for all conditions with uncertainty bars are presented in Figure 8.

16
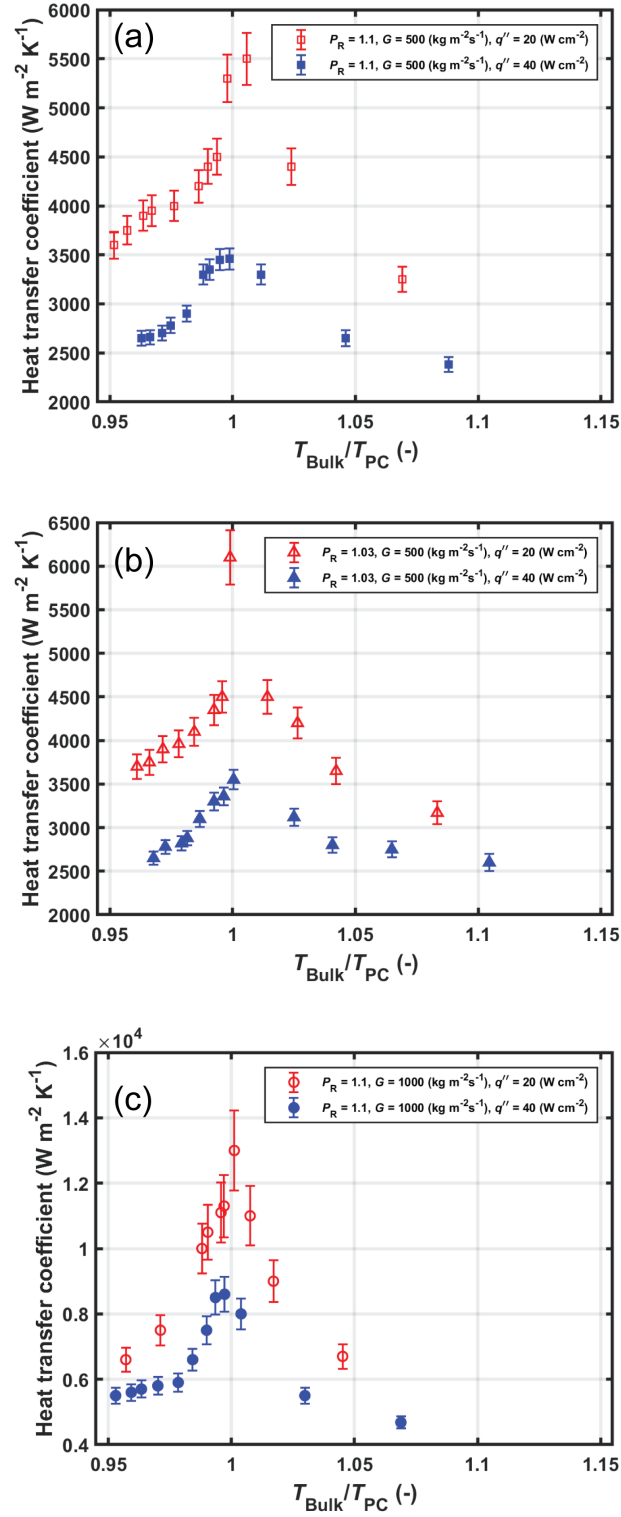
Figure 8: Average heat transfer coefficients as a function of ratio of the bulk fluid temperature and the pseudo-critical temperature.(a)$G = 500$ kg m^{-2}s^{-1} and $P_R = 1.1$(b)$G = 500$ kg m^{-2}s^{-1} and $P_R = 1.03$ (c) $G = 1000$ kg m^{-2}s^{-1} and $P_R = 1.1$

17

For all the experimental test cases, the qualitative trends in the heat transfer coefficients are identical to the variations in the values of the specific heat capacity and Prandtl number of supercritical carbon dioxide as a function of the bulk temperature and reduced pressure. The heat transfer coefficients increase with an increase in the bulk fluid temperature and reach peak values when the ratio, T_{Bulk}/T_{PC} is unity. As the bulk fluid temperature exceeds the pseudo-critical temperature, there is a monotonic decrease in the average heat transfer coefficients. Increasing the heat flux causes an attenuation in peak values of the average heat transfer coefficients and an increase in the average bottom wall temperatures as shown in figure 9. For a nominal case of $G = 1000$ kg m^{-2} s^{-1} at the 40 W cm^{-2} heat flux, the peak heat transfer coefficient is 8600 W m^{-2} K^{-1} with a corresponding average bottom wall temperature of 44.28ºC. This heat transfer coefficient increases to 13000 W m^{-2} K^{-1} when the applied heat flux is reduced to 20 W cm^{-2} with the corresponding average bottom wall temperature dropping to 39.2ºC.
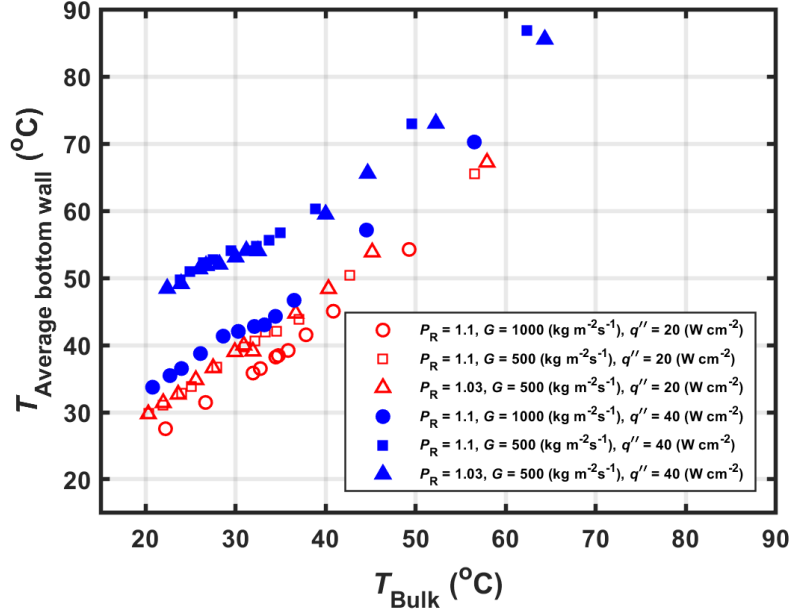

Figure 9: Channel bottom wall temperatures as a function of the bulk fluid temperature

It is generally agreed upon that an increase in sCO$_2$ mass flux will yield increases in heat transfer coefficients for macroscale hydraulic diameter tubes [31]–[35]. A 100 % increase in mass flux, as seen in Figure 8 results in a 136% and 149% increase in heat transfer coefficient when the bulk fluid temperature approaches the pseudo-critical temperature for the same thermal conditions for applied heat flux of 40 W cm^{-2} and 20 W cm^{-2}, respectively .

A decrease in reduced pressure increases the gradient of thermophysical properties with changing temperature near the critical point. In the present study, the peak heat transfer coefficients are approximately 11% higher for a reduced pressure of 1.03 at an applied heat flux of 20 W cm^{-2}. However, for the heat flux of 40 W cm^{-2}, the increase in the heat transfer coefficient at a lower reduced pressure is within experimental uncertainty. The

observed increase is consistent with most studies in literature that have observed a decrease in reduced pressure will yield a higher heat transfer coefficient.[12], [33], [36]. A summary of all of the data is shown in Figure 10. The mass flux of 1000 kg m^{-2}s^{-1} yields the highest heat transfer coefficients near the pseudo-critical temperature for both the 20 and 40 W cm^{-2} cases. It is also interesting to note that as the bulk fluid temperature exceeds the pseudo-critical temperature, the heat transfer coefficients for the same mass flux begin to overlap one-another regardless of the heat flux conditions and reduced pressure conditions. This is explained by the decrease in thermophysical property variations away from the pseudo-critical temperature point and a collapse to single phase, constant property turbulent convective heat transfer behavior. Before any attempt is made to qualify an explanation for the observed trends in the heat transfer coefficients, the effects of buoyancy and flow acceleration on the heat transfer need to be quantified.
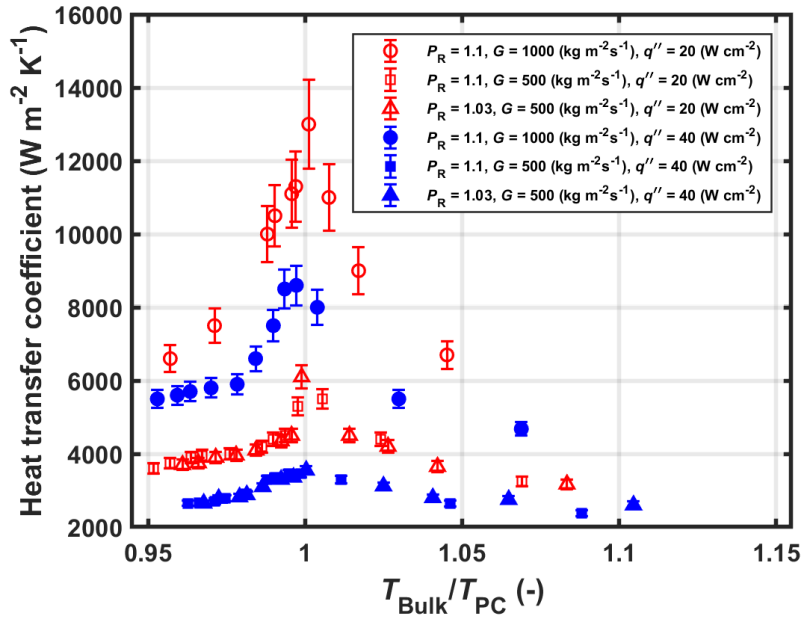

Figure 10: Trends in the average heat transfer coefficients as a function of the ratio of the bulk fluid temperature and the pseudo-critical temperature.

4.4. Quantifying Buoyancy Effects in Experiments

Experimentally determined heat transfer data must be screened for the presence of buoyancy effects to allow for an objective comparison against correlations that do not account for buoyancy forces in the flow field [37]. In the present study, the horizontal orientation of the test section with the applied heat flux at the bottom wall of the flow channel may lead to unstable thermal stratification. Unstable thermal stratification tends to enhance the heat transfer by inducing secondary flow patterns, which allow for mixing of momentum and thermal energy [14], [19], [38]. However, if a stably stratified flow were to develop in

the channel, it can interrupt these secondary flow patterns and might cancel out the enhancement in heat transfer [14]. Additionally, stably stratified flows over a heat transfer surface can inhibit the turbulent transport of momentum and thermal energy[10], [39]. In this investigation, there is some heat leakage to the test section top cover (16% of the total heat duty for 20 W cm⁻² and 16.5 % for 40 W cm⁻²) which heats up the fluid at the top of the flow channel. Average top wall temperatures predicted by COMSOL simulations are always higher than the bulk fluid temperature, which can lead to formation of a layer of stably stratified fluid at the top of the test section flow channel. The relative thickness of this stably stratified fluid layer in comparison to the unstable stratification at the bottom of the flow channel will ultimately determine whether enhanced or deteriorated heat transfer is observed.

At present, we do not have the means to visually inspect the influence of these competing mechanisms on the heat transfer but it is still useful to quantify the potential effects of buoyancy forces on our experimental data. For supercritical fluids, several different criteria have been proposed in the literature to gauge the influence of buoyancy forces on the heat transfer performance [40]. However, there is no consensus in the research community regarding the most suitable buoyancy criterion for a given flow geometry and heat flux boundary conditions.

For turbulent mixed convection in horizontal flows, Petukhov and Polyakov [19] propose a threshold Grashof (Gr_{th}) number which quantifies the strength of the buoyancy forces affecting the whole flow field and thereby causing a 1% deviation in the Nusselt number from that of pure forced convective heat transfer. This threshold Grashof number is defined in equation 7. The standard Grashof number defined by equation 1 determines the magnitude of the buoyancy forces in the flow field and to gauge the significance of these buoyancy forces on the heat transfer, the relative magnitudes of the two Grashof numbers as defined by equations 1 and 7 need to be compared.

$$Gr_{th} = 3 \times 10^{-5} Re_b^{2.75} \bar{Pr} \left[1 + 2.4 Re^{-\frac{1}{8}} \left(\bar{Pr}^{\frac{2}{3}} - 1 \right) \right] \tag{7}$$

$$\bar{Pr} = \frac{h_w - h_b}{T_w - T_b} \frac{\mu_b}{k_b} \tag{8}$$

The Grashof number defined earlier in equation (1) can be expressed in an alternative form as shown in equation 9. This expression is derived using the definition of heat flux where $\bar{\beta}$ is defined in equation 10

$$Gr_q = \frac{g \bar{\beta} q'' D_H^4}{\nu_b^2 k_b} \tag{9}$$

$$\bar{\beta} = \frac{1}{\rho_{film}} \frac{\rho_b - \rho_w}{T_w - T_b} \tag{10}$$

Typically, the ratio of Gr_q and Gr_{th} is evaluated to quantify the effects of buoyancy forces on the heat transfer performance [13], [19]. When buoyancy forces do not significantly influence the heat transfer, the ratio of these two Grashof number should be unity.
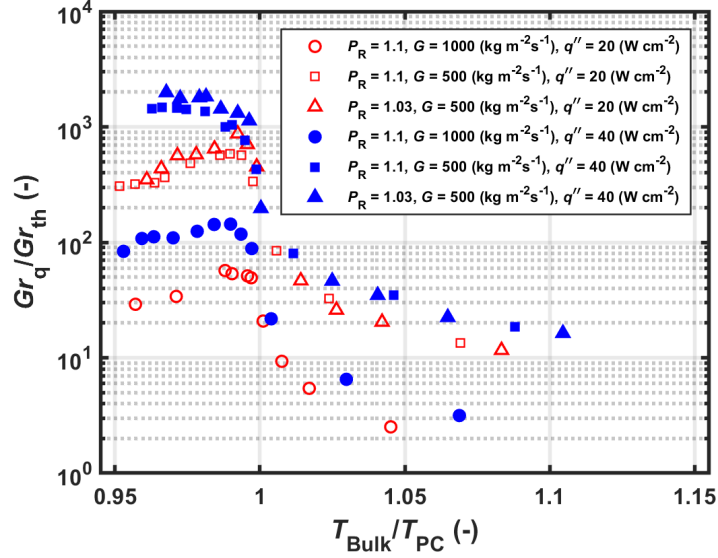
Figure 11: Ratio of the Grashof numbers as a function of the ratio of the bulk fluid temperatures and the pseudo-critical temperature.

Bottom wall average temperatures predicted by the COMSOL Multiphysics simulation and experimentally measured bulk fluid temperatures and heat flux were used to calculate the parameters defined in the equations 7 through 10. According to Bazargan et $al.$ [13] the choice of top wall or the bottom wall temperatures should not matter in the evaluation of these parameters. For all the experimental test cases, the ratio Gr_q/Gr_{th} as a function of the ratio, T_{Bulk}/T_{PC} is shown in Figure 11.

Based on these trends, it is evident that the magnitude of the buoyancy forces in the flow field is sufficiently strong enough to influence the heat transfer behavior of sCO$_2$ near the pseudo-critical temperature. In particular, buoyancy effects become more prominent as a consequence of a large density gradient when the condition $T_b < T_{pc} < T_w$ is true . The ratio of the two Grashof numbers varies from 2.52 to a maximum value of 1986. As the bulk fluid temperature increases beyond the pseudo-critical point, this ratio approaches values close to unity which is indicative of pure forced convective heat transfer behavior in that temperature regime. In general, regardless of the heat flux and the system reduced pressure, experimental test cases for a mass flux of 1000 kg m^{-2} s^{-1} appear to be less affected by buoyancy when compared to cases for the mass flux of 500 kg m^{-2} s^{-1}. In particular, the test case for a mass flux of 1000 kg m^{-2}s^{-1} and a heat flux of 20 W cm^{-2} had the least effects of buoyancy on the heat transfer. The maximum value of the ratio, Gr_q/Gr_{th} for this particular case was 56.97, which increased to 586.4 for a mass flux of 500 kg m^{-2} s^{-1} for the same applied heat flux. An increase in the relative magnitude of the inertial forces as compared to the buoyancy forces at higher mass flow rates is a possible explanation of this observed trend.

21

4.5. Quantifying Flow Acceleration

An axial decrease in the bulk fluid density of the fluid as a consequence of the applied heat flux causes an increase in the bulk fluid velocity in order to satisfy the mass continuity. An increase in the mean fluid velocity will result in a favorable pressure gradient being imposed on the turbulent boundary layer which will cause an increase in the thickness of the viscous sub-layer and overall reduction in the thickness of the turbulent boundary layer [9]. An increase in the thickness of the viscous-sublayer will increase the resistance to the thermal transport from the wall to the bulk of the fluid but of greater consequence is the *re-laminarization* of the entire turbulent boundary layer due to the favorable pressure gradient. If that were to happen, there would be a sharp deterioration in the heat transfer performance and correlations developed for heat transfer in turbulent flows would always over-predict the magnitude of the thermal transport.

Research effort by J.D.Jackson [6], [7], [21] has led to the development of heat transfer correlations for supercritical flows which take into account the influence of flow acceleration. The approach used in his research is based on the end goal of relating the effect of a favorable pressure gradient on the reduction of the shear stress in the turbulent boundary layer in terms of the applied heat flux, bulk fluid velocity, buffer layer thickness and thermophysical properties evaluated at the bulk fluid temperature. Once the reduction in the shear stress is expressed in terms of measurable flow and heat transfer variables, the corresponding reduction in the heat transfer is expressed by exploiting the dependence of both the Nusselt number and the friction factor on the Reynolds number as expressed by conventional correlations developed for turbulent pipe flow. In the process of developing these correlations, threshold criteria were also proposed which can be used to screen the experimental data for the presence of thermally induced bulk flow acceleration. It is imperative to note that these criteria and correlations were developed for uniformly applied heat flux boundary conditions, which is not the case in the present investigation. Following the notation used by J.D.Jackson [6], the acceleration parameter is defined as follows:

$$\psi = C_A A_{cb} F_{VP1} \tag{11}$$

$$C_A = 10^4 \tag{12}$$

$$A_{cb} = \frac{\beta_b q_w'' D}{k_b Re_b^{1.625} Pr_b} \tag{13}$$

$$F_{VP1} = \left(\frac{\mu_{ave}}{\mu_b}\right)\left(\frac{\rho_{ave}}{\rho_b}\right)^{-0.5} \tag{14}$$

When the value of ψ is below 0.385, reduction in heat transfer as a consequence of bulk flow acceleration will be less than 2%.

For all the experimental test cases, the acceleration parameter, ψ as a function of the the ratio, T_{Bulk}/T_{PC} is shown in Figure 12. In accordance with Jackson's acceleration threshold criteria, bulk flow acceleration is affecting the heat transfer performance in all the experimental test cases except for the one with a mass flux of 1000 kg m^2 s^{-1} and a heat flux of 20 W cm^{-2}. These results are to be interpreted with caution because as mentioned
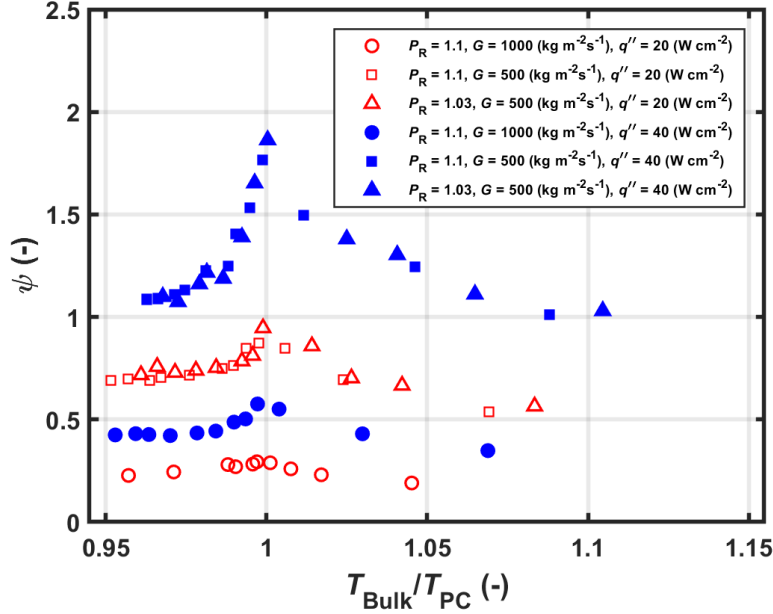
22

Figure 12: Acceleration parameter as a function of the ratio of the bulk fluid temperatures and the pseudo-critical temperature.

earlier, this particular criterion is applicable for uniformly applied heat flux. In the present study, the heat flux of 20 W cm^{-2} and 40 W cm^{-2} is only applied to single boundary of the flow channels and is limited to the 20 mm "heated length" of the test section.

4.6. Comparison with Literature

Experimental data is compared against three empirical supercritical correlations and the Dittus-Boelter correlation developed for subcritical, constant property, single-phase, turbulent flow conditions. The details of these correlations are summarized in Table 5.

The general form of the Jackson and Hall [41] correlation is similar to the Dittus-Boelter correlation with additional property ratio terms. These property ratios are intended to account for the drastic property variations by calculating properties at wall and bulk fluid temperature. The Kruizenga et al. [16] correlation modifies the Jackson and Hall [41] correlation by incorporating a specific heat ratio correction term. The correlation proposed by Liao and Zhao [18] includes an additional buoyancy parameter of the form $\frac{Gr}{Re^2}$ (i.e., the Richardson number). These correlations are compared based on the mean absolute percent error (MAPE) and the ratio, R_α between the predicted value from the correlations (α_{corr}) and experimental value (α_{exp}).

$$MAPE = \frac{100\%}{N} \sum_{i=1}^{N} \left| \frac{\alpha_{exp} - \alpha_{corr}}{\alpha_{exp}} \right| \tag{15}$$

$$R_\alpha = \frac{\alpha_{corr}}{\alpha_{exp}} \tag{16}$$

23

The $MAPE$ and R_α values for different test conditions are summarized in Tables 6 and 7, respectively.

The comparison of the experimental data against the Dittus-Boelter correlation, with the Reynolds and Prandtl numbers evaluated at the bulk fluid temperature, is shown in Figure 13a. For all the experimental test cases in this study, the Dittus-Boelter correlation over-predicts the heat transfer coefficients when the ratio, T_{Bulk}/T_{PC} is between 0.99 - 1.01. The disagreement of the experimental data with the correlation decreases on either side of the pseudo-critical point, as indicated by the $MAPE$ values in table 6. To interpret the results of this comparison, it is helpful if the turbulent boundary layer can be thought of having two distinct regions with different thermal resistance values. The near wall, viscous sub-layer region where diffusive mechanisms dominate the thermal transport, will offer the highest resistance to the heat transfer from the wall to the bulk of the fluid. Experimental test conditions with a combination of low mass flux (500 kg m^{-2} s^{-1}) and higher heat flux (40 W cm^{-2}) lead to a difference between bottom average wall temperature and the bulk fluid temperature as high as 22ºC near the pseudo-critical point. This makes the resistance of the viscous sub-layer, with its poor thermophysical properties, the limiting resistance to the heat transfer. Therefore, the Dittus-Boelter correlation with its dimensionless parameters evaluated at the bulk fluid temperature will always over-predict the heat transfer coefficient. However, this is not to say that possible influence of buoyancy and flow acceleration on the heat transfer can be ignored, but rather it is the combination of all three factors which can explain the observed disagreement.

In the present configuration of the experimental test section, the buoyancy forces would induce secondary flow in the microchannels which should lead to an enhancement in the heat transfer[14]. However, as mentioned in the previous section, the heat leakage to the test section top cover can lead to stably stratified flow at the top surface of the flow channel which can negate this potential enhancement. Moreover, flow acceleration, if significant enough to cause the *re-laminarization* of the turbulent boundary layer will always lead to a deterioration in the heat heat transfer. Therefore, due to simultaneous influence of these phenomena, it is difficult to pinpoint the exact mechanism for the observed disagreement between the experimental data and the predictions by the Dittus-Boelter correlation. However, for the experimental test case with a mass flux of 1000 kg m^{-2}s^{-1} and a heat flux of 20 W cm^{-2}, the effects of flow acceleration on the heat transfer can be ignored. This is due to the acceleration parameter, ψ, never exceeding its threshold value of 0.385. For this particular test case, the experimentally determined heat transfer coefficients are higher (not within uncertainty) than those predicted by the Dittus-Boelter correlation when the ratio, T_{Bulk}/T_{PC} is less than 1. This enhancement can be explained due to secondary flow patterns as a consequence of buoyancy forces as observed by [14] or due to a low value of the near wall thermal resistance. A look at the wall temperatures for this temperature regime indicates that they range from 27ºC to 35.86ºC and will result in enhanced thermal transport properties in the viscous sub-layer which can contribute to the observed enhancement. However, the experimentally determined heat transfer coefficients are still higher than those predicted by the Dittus-Boelter correlation when the ratio, T_{Bulk}/T_{PC} is larger than 1. This enhancement cannot be explained by a decrease in the resistance offered by the sub-layer

24

Table 5: Details of the correlations used for comparison against experimental data.

Authors	Correlation	Conditions/Comments
[41]	$Nu_b = 0.0183 Re_b^{0.82} pr_b^{0.5} \left(\frac{\rho_w}{\rho_b}\right)^{0.3} \left(\frac{\bar{C}_p}{C_{p,b}}\right)^n$ $\bar{C}_p = \frac{h_w - h_b}{T_w - T_b}$ $n = 0.4$ if $T_b < T_w < T_{PC}$ or $1.2 T_{PC} < T_b < T_w$ $n = 0.4 + 0.3\left(\frac{T_w}{T_{pc}} - 1\right)$ if $T_b < T_{PC} < T_w$ $n = 0.4 + 0.2\left(\frac{T_w}{T_{pc}} - 1\right)\left[1 - 5\left(\frac{T_w}{T_{pc}} - 1\right)\right]$ if $T_{PC} < T_B < 1.2 T_{PC}$ and $T_b < T_w$	Modified[42]
[18]	$Nu_b = 0.124 Re_b^{0.8} Pr_b^{0.4} \left(\frac{Gr_b}{Re_b^2}\right)^{0.203} \left(\frac{\rho_w}{\rho_b}\right)^{0.842} \left(\frac{\bar{C}_p}{C_{p,b}}\right)^{0.384}$ $Gr_b = \frac{(\rho_b - \rho_w)\rho_b g D_H^3}{\mu_b^2}$ $\bar{C}_p = \frac{h_w - h_b}{T_w - T_b}$	$0.9 \leq Pr \leq 10$ $10^4 \leq Re \leq 2 \times 10^5$ $7.4 \leq P \leq 12$ Mpa $20 \leq T_b \leq 110$ºC $0.02 \leq \dot{m} \leq 0.2$kg min⁻¹ $1 \leq q'' \leq 20$ W cm⁻² $0.7 \leq D_H \leq 2.16$ mm sCO₂ heating and horizontal tube
[16]	$Nu_b = Nu_{Jack}\left(\frac{\bar{C}_{p,b}}{C_{p,b-IG}}\right)^{-0.19}$	$0.9 \leq Pr \leq 10$ $Re \leq \times 10^5$ $7.5 \leq P \leq 10.2$ Mpa $326 \leq G \leq 1197$ kg m⁻²s⁻¹ $D_H = 1.16$ mm sCO₂ cooling and horizontal channels
[43]	$Nu_b = 0.023 Re_b^{0.8} Pr_b^{0.4}$	$0.7 \leq Pr \leq 16$ $Re \leq 10000$ $L/D \geq 10$ Water and subcritical

because the wall temperatures are higher than 45ºC ($T_{PC} = 35.83ºC$). The only plausible reason for enhancement in this temperature regime can be attributed to the buoyancy forces as the ratio, $\frac{Gr_q}{Gr_{th}}$ is still higher than unity for this temperature regime.

The predictive capability of the three supercritical correlations as characterized by R_α values is shown in Figure 13 (b)-(d). The Jackson and Hall [41] correlation is developed to account for the effects of variable thermophysical properties on the heat transfer but it does not incorporate the influence of buoyancy and flow acceleration on thermal transport. Due to the inclusion of the property ratio correction terms to the Dittus-Boelter type correlation, it is expected that the predictive capability of the Jackson and Hall correlation will be better than the Dittus-Boelter correlation when the ratio, T_{Bulk}/T_{PC}, ranges between 0.99 - 1.01. This is indeed the case as indicated by the $MAPE$ values in table 6. The experimental test case (G = 1000 kg m⁻²s⁻¹ and q” = 20 W cm⁻²) had the best agreement with the Jackson and Hall correlation with a $MAPE$ of 32% across the entire temperature range. As mentioned earlier, flow acceleration effects were negligible for this test case and effects of buoyancy

25

were minimal as compared to other test cases. In the vicinity of the pseudo-critical point, average heat transfer coefficients predicted by the Jackson and Hall correlation are within 35% of the experimentally measured heat transfer coefficients for all the test cases.

The Kruizenga *et al.*[16] was developed for supercritical fluid flows under cooling conditions. The Jackson and Hall correlation [41] was modified by an additional specific heat ratio term to provide a good fit for their own experimental data. The intended effect of this specific heat ratio term was to reduce the Nusselt numbers predicted by the Jackson and Hall correlation and this trend is evident from figure 13 (c). The average MAPE for this correlation in the vicinity of the pseudo-critical point is 61.4%. This trend points to the fact that supercritical correlations developed for cooling boundary conditions are not able to predict the heat transfer for heating conditions with high accuracy.

The Liao and Zhao [18] correlation takes into account the effects of buoyancy and variable fluid properties on heat transfer. However, the agreement of this correlation with the experimental results of the present study is relatively poor (Average MAPE 65.87%). The agreement is worse in the region where buoyancy forces are significantly influencing the heat transfer as shown in figure 11 when the ratio, T_{Bulk}/T_{PC} is less than unity. A possible reason for this disagreement could be attributed to the fact that the correlation was developed from experimental data obtained for a uniformly heated circular tube. A consequence of this would be that the correlation is also taking into account the reduction in the heat transfer from the top surface of the tube where low density and low conductivity fluid accumulates. Even though in the present investigation, there is some heat leakage to the test section top cover, the majority of the applied heat flux ends up heating the fluid from the bottom. Therefore, the magnitude of the reduction in the heat transfer at the top of the flow channels will be relatively small in comparison to that encountered in a uniformly heated circular tube.

Table 6: *MAPE* values for supercritical and subcritical correlations

	T_b/T_{PC}	Jackson and Hall [41]	Liao and Zhao [18]	Kruizenga *et al.* [16]	Dittus and Boelter [43]
	< 0.99	38.32	63.81	53.6	5.76
20 Wcm⁻²	0.99 - 1.01	34.9	59.11	61.12	39.6
	> 1.01	45.2	58.61	57.3	13.93
	< 0.99	41.25	81.7	56.08	34.43
40 Wcm⁻²	0.99 - 1.01	35.07	68.86	61.72	121.9
	> 1.01	39.19	63.1	50.15	31.3
Average	-	38.9	65.87	56.58	41.15

Table 7: R_α values for supercritical and subcritical correlations

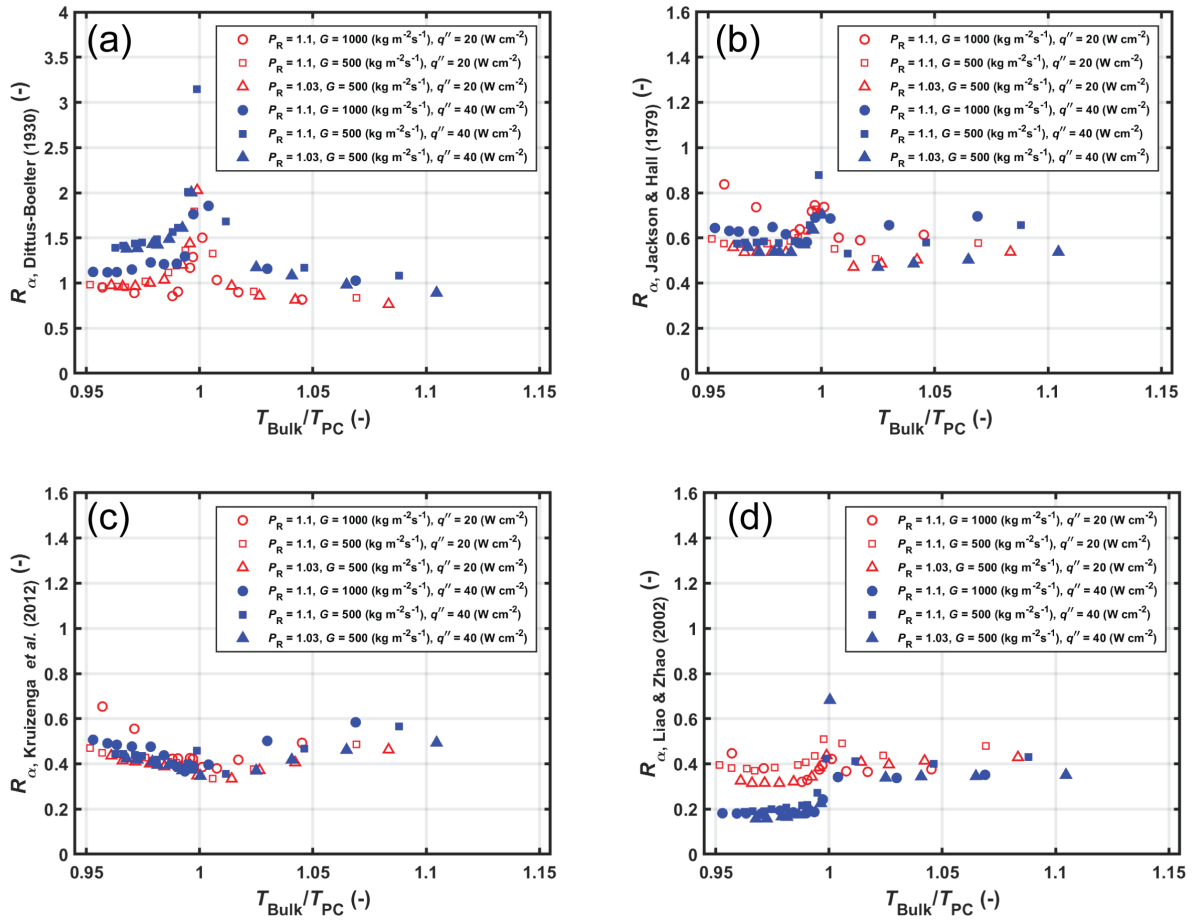|	T_b/T_{PC}	Jackson and Hall [41]	Liao and Zhao [18]	Kruizenga *et al.* [16]	Dittus and Boelter [43]
	< 0.99	0.61	0.36	0.46	0.95
20 Wcm⁻²	0.99 - 1.01	0.65	0.56	0.38	1.38
	> 1.01	0.54	0.41	0.42	0.86
	< 0.99	0.58	0.18	0.44	1.34
40 Wcm⁻²	0.99 - 1.01	0.64	0.31	0.38	2.21
	> 1.01	0.60	0.5	0.37	1.1
Average	-	0.60	0.39	0.41	1.30

Figure 13: Comparison of experimental data against correlations.(a) R_α Dittus-Boelter correlation. [41] correlation.(b) R_α Jackson and Hall [41] correlation. (c) R_α for Kruizenga *et al.* [16].(d) R_α for Liao and Zhao [18] correlation.

5. Conclusions

The present study investigated the heat transfer characteristics of supercritical carbon dioxide in a multi-parallel microchannel heat exchanger operating in a horizontal flow configuration. The hydraulic diameter of the channels was 0.75 mm with an aspect ratio of one. Unlike previous studies, the heat flux boundary condition was not uniform across the flow periphery but was limited to a single bottom wall surface of the test section. Experiments were conducted over a range of heat fluxes ($20 \leq q'' \leq 40$ W cm^{-2}), mass fluxes ($500 \leq G \leq 1000$ kg m^{-2} s^{-1}), reduced pressure ($1.03 \leq P_R \leq 1.1$), and inlet temperatures ($16 \leq T_{in} \leq 50$ °C). A data analysis methodology that involved the development and integration of a 2D resistance network model and a 3D FEA heat transfer model of the test section was used to calculate the average heat transfer coefficients in the test section and quantify experimental uncertainty.

For all the experimental test cases, the qualitative trends in the heat transfer coefficients are identical to the variations in the values of the specific heat capacity and Prandtl number of supercritical carbon dioxide as a function of the bulk temperature and reduced pressure. The heat transfer coefficients increase with an increase in the bulk fluid temperature and reach peak values when the ratio, T_{Bulk}/T_{PC} is unity. As the bulk fluid temperatures exceed the pseudo-critical temperature, there is a monotonic decrease in the average heat transfer coefficients. Increasing the heat flux causes an attenuation in peak values of the average heat transfer coefficients. For the same applied heat flux, an increase in the mass flux will cause an increase in the average heat transfer coefficient. These general trends are in agreement with prior work.

Potential effects of buoyancy forces on heat transfer in horizontal flow geometries were quantified by a criterion proposed by Petukhov and Polyakov [19]. Based on this criterion, buoyancy forces significantly influenced the heat transfer performance of the supercritical carbon dioxide in the vicinity of the critical point. Heat transfer enhancement, potentially due to unstable flow stratification that was not within experimental uncertainty was only observed for the test case ($G = 1000$ kg m^{-2}s^{-1}, $P_R = 1.1$ and $q'' = 20$ W cm^{-2}) for $T_{Bulk} < T_{PC}$. Effects of bulk flow acceleration on the heat transfer performance of supercritical carbon dioxide were quantified by using the criterion proposed by J.D.Jackson. Based on this analysis, it was concluded that bulk flow acceleration was significant enough to cause heat transfer deterioration for the majority of the experimental data points.

For all the experimental test cases, the Jackson and Hall [41] correlation was able to predict the heat transfer fairly well (MAPE $\simeq 35\%$) when T_{Bulk}/T_{PC} ranged from 0.99 - 1.01. For the temperatures in the vicinity of the critical point, Dittus-Boelter correlation always over-predicted the heat transfer coefficients. This was attributed to the simultaneous effect of buoyancy, flow acceleration and large thermal resistance of viscous sub-layer in that temperature regime. The supercritical correlations developed for cooling conditions failed to predict the heat transfer data of the present study with reasonable accuracy. The only correlation evaluated in the present study that accounted for buoyancy forces and developed for heating conditions in microscale geometries was that of Liao and Zhao [18]. However, this correlation had the worst agreement ($MAPE \simeq 65.87\%$) with the experimental data

among the three correlations developed for supercritical flows that were evaluated in the present study. One of the reasons for the not so stellar performance of the supercritical correlations used in the present study could be attributed to the fact that all of them were developed for uniformly applied heat flux boundary conditions. This is not the case in the present study.

Although, buoyancy and flow acceleration effects were potentially influencing the heat transfer in the present investigation, this conclusion is based on the results of the screening criteria developed for circular and uniformly heated flow channels. This is in contrast to the operating conditions in the current investigation. This calls for a systematic investigation for the confirmation of both buoyancy and flow acceleration effects under non-uniform heating conditions in microscale heat transfer geometries, and the development of criterion to predict their onset.

6. Acknowledgments

References

[1] K. R. Zada, M. B. Hyder, M. Kevin Drost, and B. M. Fronk, "Numbering-Up of Microscale Devices for Megawatt-Scale Supercritical Carbon Dioxide Concentrating Solar Power Receivers," *Journal of Solar Energy Engineering*, vol. 138, no. 6, p. 061 007, 2016, ISSN: 0199-6231. DOI: 10.1115/1.4034516. [Online]. Available: http://solarenergyengineering.asmedigitalcollection.asme.org/article.aspx?doi=10.1115/1.4034516.

[2] M. B. Hyder and B. M. Fronk, "Simulation of thermal hydraulic performance of multiple parallel micropin arrays for concentrating solar thermal applications with supercritical carbon dioxide," *Solar Energy*, vol. 164, no. February, pp. 327–338, 2018, ISSN: 0038092X. DOI: 10.1016/j.solener.2018.02.035. [Online]. Available: https://doi.org/10.1016/j.solener.2018.02.035.

[3] C. K. Ho and B. D. Iverson, "Review of high-temperature central receiver designs for concentrating solar power," *Renewable and Sustainable Energy Reviews*, vol. 29, pp. 835–846, 2014, ISSN: 13640321. DOI: 10.1016/j.rser.2013.08.099. [Online]. Available: http://dx.doi.org/10.1016/j.rser.2013.08.099.

[4] M. D. Carlson, A. K. Kruizenga, C. Schalamsky, and D. F. Fleming, "Sandia Progress on Advanced Heat Exchangers for SCO2 Brayton Cycles," *4th International Symposium - Supercritical CO2 Power Cycles*, 2014, ISSN: 1098-6596. DOI: 10.1017/CBO9781107415324.004.

[5] B. M. Fronk and A. S. Rattner, "High-Flux Thermal Management With Supercritical Fluids," *Journal of Heat Transfer*, vol. 138, no. 12, p. 124 501, 2016, ISSN: 0022-1481. DOI: 10.1115/1.4034053. [Online]. Available: http://heattransfer.asmedigitalcollection.asme.org/article.aspx?doi=10.1115/1.4034053.

[6] J. D. Jackson, "Fluid flow and convective heat transfer to fluids at supercritical pressure," *Nuclear Engineering and Design*, vol. 264, pp. 24–40, 2013, ISSN: 00295493. DOI: 10.1016/j.nucengdes.2012.09.040. [Online]. Available: http://dx.doi.org/10.1016/j.nucengdes.2012.09.040.

[7] ——, "Models of heat transfer to fluids at supercritical pressure with influences of buoyancy and acceleration," *Applied Thermal Engineering*, vol. 124, pp. 1481–1491, 2017, ISSN: 13594311. DOI: 10.1016/j.applthermaleng.2017.03.146. [Online]. Available: http://dx.doi.org/10.1016/j.applthermaleng.2017.03.146.

[8] J. Jackson, M. Cotton, and B. Axcell, "Studies of mixed convection in vertical tubes," *International Journal of Heat and Fluid Flow*, vol. 10, no. 1, pp. 2–15, 1989, ISSN: 0142727X. DOI: 10.1016/0142-727X(89)90049-0.

[9] W. M. Kays and M. Crawford, *Convective Heat and Mass Transfer*, 2nd ed. McGraw-Hill, 1980, pp. 182–183.

[10] S. Arya, "Buoyancy effects in a horizontal flat-plate boundary layer," *Journal of Fluid Mechanics*, vol. 68, pp. 321–343, 1975.

[11] G. Adebiyi W.B. Hall, "Experimental Investigation of Heat Transfer to supercritical pressure carbon dioxide in a horizontal pipe," *International Journal of Heat and Mass Transfer*, vol. 19, pp. 715–720, 1976.

[12] S. R. Pidaparti, J. A. McFarland, M. M. Mikhaeil, M. H. Anderson, and D. Ranjan, "Investigation of Buoyancy Effects on Heat Transfer Characteristics of Supercritical Carbon Dioxide in Heating Mode," *J. Nuclear Engineering and Radiation Science*, vol. 1, no. 3, pp. 1–10, 2015, ISSN: 2332-8983. DOI: 10.1115/1.4029592.

[13] M. Bazargan, D. Fraser, and V. Chatoorgan, "Effect of Buoyancy on Heat Transfer in Supercritical Water Flow in a Horizontal Round Tube," *Journal of Heat Transfer*, vol. 127, no. 8, p. 897, 2005, ISSN: 00221481. DOI: 10.1115/1.1929787.

[14] J. Wang, Z. Guan, H. Gurgenci, K. Hooman, and A. Veeraragavan, "Computational investigations of heat transfer to supercritical CO 2 in a large horizontal tube," *Energy Conversion and Management*, vol. 157, no. December 2017, pp. 536–548, 2018, ISSN: 0196-8904. DOI: `10.1016/j.enconman.2017.12.046`. [Online]. Available: `https://doi.org/10.1016/j.enconman.2017.12.046`.

[15] A. Kruizenga, M. Anderson, R. Fatima, M. Corradini, A. Towne, and D. Ranjan, "Heat Transfer of Supercritical Carbon Dioxide in Printed Circuit Heat Exchanger Geometries," *Journal of Thermal Science and Engineering Applications*, vol. 3, no. 3, p. 031 002, 2011, ISSN: 19485085. DOI: `10.1115/1.4004252`. [Online]. Available: `http://thermalscienceapplication.asmedigitalcollection.asme.org/article.aspx?articleid=1469777`.

[16] A. Kruizenga, H. Li, M. Anderson, and M. Corradini, "Supercritical Carbon Dioxide Heat Transfer in Horizontal Semicircular Channels," *Journal of Heat Transfer*, vol. 134, no. 8, p. 081 802, 2012, ISSN: 00221481. DOI: `10.1115/1.4006108`. [Online]. Available: `http://heattransfer.asmedigitalcollection.asme.org/article.aspx?articleid=1450565`.

[17] C.-y. Yang, "Icnmm2015-48212 Heat Transfer Performance of Supercritical Carbon Dioxide in," pp. 1–7, 2016.

[18] S. M. Liao and T. S. Zhao, "Measurements of Heat Transfer Coefficients From Supercritical Carbon Dioxide Flowing in Horizontal Mini/Micro Channels," *Journal of Heat Transfer*, vol. 124, no. 3, p. 413, 2002, ISSN: 00221481. DOI: `10.1115/1.1423906`.

[19] B. Petukhov and A. Polyakov, *Heat Transfer in Turbulent Mixed Convection*, B. Launder, Ed. Hemisphere Publishing Corporation, 1988, ISBN: 0-89116-644-0.

[20] S. M. Liao and T. S. Zhao, "An Experimental Investigation of Convective Heat Transfer to Supercritical Carbon Dioxide in Minature Tubes," *Int. J. Heat*, vol. 45, no. 25, pp. 5025–5034, 2002, ISSN: 00179310. DOI: `10.1016/S0017-9310(02)00206-5`.

[21] J. D. Jackson, "Heat transfer deterioration in tubes caused by bulk flow acceleration due to thermal and frictional influences," pp. 223–230, 2012.

[22] D. M. McEligot and J. D. Jackson, ""Deterioration" criteria for convective heat transfer in gas flow through non-circular ducts," *Nuclear Engineering and Design*, vol. 232, no. 3, pp. 327–333, 2004, ISSN: 00295493. DOI: `10.1016/j.nucengdes.2004.05.004`.

[23] A. Agarwal and S. Garimella, "Representative Results for Condensation Measurements at Hydraulic Diameters fffdfffdfffd100fffdfffdfffdMicrons," *Journal of Heat Transfer*, vol. 132, no. 4, p. 041 010, 2010, ISSN: 00221481. DOI: `10.1115/1.4000879`. [Online]. Available: `http://heattransfer.asmedigitalcollection.asme.org/article.aspx?articleid=1449896`.

[24] S. Garimella, A. Agarwal, and B. M. Fronk, "Condensation heat transfer in rectangular microscale geometries," *International Journal of Heat and Mass Transfer*, vol. 100, pp. 98–110, 2016, ISSN: 00179310. DOI: `10.1016/j.ijheatmasstransfer.2016.03.086`. [Online]. Available: `http://dx.doi.org/10.1016/j.ijheatmasstransfer.2016.03.086`.

[25] COMSOL AB, *COMSOL Multiphysics v. 5.1./5.2.* Stockholm, 2016.

[26] C. Ho and T. Chu, "Electrical Resistivity and Thermal Conductivity of Nine Selected AISI Stainless Steels," Centre for Information, Numerical Data Anaysis, and Synthesis. Purdue Indistrial Research Park, Tech. Rep., 1977.

[27] R. Span and W. Wagner, "A new Equation of State for Carbon Dioxide Covering the Fluid Region from the Triple-Point Temperature of 1100 K at Pressure up to 800 mpA.," *Journal of Physical and Chemical Reference Data*, vol. 25, no. 6, pp. 1509–1596, 1996.

[28] S. Kline and F. Mcclintock, "Describing Uncertainties in Single-Sample Experiments," *Mechanical Engineering*, vol. 75, pp. 3–8, 1953.

[29] S. Klein, *F-Chart Software: EES, V10.104*, Madison, 2016.

[30] S. A. Jajja and B. M. Fronk, "Supercritical Carbon Dioxide Heat Transfer Data for 0.75 mm Square Microchannels with Horizontal, Single-Side Heated Boundary Condition at Reduced Pressure from 1.03 to 1.1," 2018. DOI: `https://doi.org/10.6084/m9.figshare.7144247.v1`. [Online]. Available: `https://doi.org/10.6084/m9.figshare.7144247.v1`.

[31] H. Kim, Y. Y. Bae, H. Y. Kim, and J. H. Song, "Exprimental Investigation on the Heat Transfer Characteristics in Upward FLow of Supercritical Carbon Dioxide," *Nucl. Technol.*, vol. 164, no. 1, pp. 119–129, 2007.

[32] H. Kim, H. Y. Kim, J. H. Song, and Y. Y. Bae, "Heat Transfer to Supercritical Pressure Carbon Dioxide Flowing Upward Through Tubes and a Narrow Annulus Passage," *Prog. Nucl. Energ.*, vol. 50, no. 2-6, pp. 518–525, 2008, ISSN: 01491970. DOI: `10.1016/j.pnucene.2007.11.065`.

[33] Y.-y. Bae, H.-y. Kim, and D.-j. Kang, "Forced and mixed convection heat transfer to supercritical CO 2 vertically flowing in a uniformly-heated circular tube," *Experimental Thermal and Fluid Science*, vol. 34, no. 8, pp. 1295–1308, 2010, ISSN: 0894-1777. DOI: `10.1016/j.expthermflusci.2010.06.001`. [Online]. Available: `http://dx.doi.org/10.1016/j.expthermflusci.2010.06.001`.

[34] D. E. Kim and M. H. Kim, "Experimental study of the effects of flow acceleration and buoyancy on heat transfer in a supercritical fluid flow in a circular tube," *Nuclear Engineering and Design*, vol. 240, no. 10, pp. 3336–3349, 2010, ISSN: 00295493. DOI: `10.1016/j.nucengdes.2010.07.002`. [Online]. Available: `http://dx.doi.org/10.1016/j.nucengdes.2010.07.002`.

[35] H. Zahlan, D. Groeneveld, and S. Tavoularis, "Measurements of Convective Heat Transfer to Vertical Upward Flows of CO2 in Circular Tubes at Near-Critical and Supercritical Pressures," *Nuc*, vol. 289, pp. 92–107, 2015, ISSN: 00295493. DOI: `10.1016/j.nucengdes.2015.04.013`.

[36] K. Tanimizu and R. Sadr, *Experimental Investigation of Buoyancy Effects on Convection Heat Transfer to Supercritical CO2 Flow in a Horizontal Tube*, 2015.

[37] J. D. Jackson, "Screening and Correlating Data on Heat Transfer to Fluids at Supercritical Pressure," *Journal of Nuclear Engineering and Radiation Science*, vol. 2, no. 1, p. 011 001, 2015, ISSN: 2332-8983. DOI: `10.1115/1.4031378`. [Online]. Available: `http://nuclearengineering.asmedigitalcollection.asme.org/article.aspx?doi=10.1115/1.4031378`.

[38] A. Elatar and K. Siddiqui, "The influence of bottom wall heating on the mean and turbulent flow behavior in the near wall region during mixed convection," *International Journal of Thermal Sciences*, vol. 77, pp. 233–243, 2014, ISSN: 12900729. DOI: `10.1016/j.ijthermalsci.2013.11.001`. [Online]. Available: `http://dx.doi.org/10.1016/j.ijthermalsci.2013.11.001`.

[39] D. Osborne and F. Incropera, "Experimental study of mixed convection heat transfer for transitional and turbulent flow between horizontal,parallel plates.," *International Journal of Heat and Mass Transfer*, vol. 28, pp. 1337–1344, 1985.

[40] D. Huang and W. Li, "A brief review on the buoyancy criteria for supercritical fluids," *Applied Thermal Engineering*, vol. 131, pp. 977–987, 2018, ISSN: 13594311. DOI: `10.1016/j.applthermaleng.2017.12.042`. [Online]. Available: `https://doi.org/10.1016/j.applthermaleng.2017.12.042`.

[41] J. Jackson and W. Hall, "Forced Convection Heat Transfer to Fluids at Supercritical Pressure," *Turublent Forced Convection in Channels and Bundles*, vol. 2, pp. 563–611, 1979.

[42] E. Krasnoshchekov and V. Protopopov, "Experimental Study of Heat Exchange in Carbon Dioxide in teh Supercritical Region at High Temperature Drops," *High Temp.+*, vol. 4, no. 3, pp. 375–382, 1966.

[43] F. W. Dittus and L. Boelter, "Heat Transfer in Automobile Radiators of the Tubular Type," University of California, Tech. Rep. 13, 1930, pp. 443–461.

List of Figures

List of Tables

Nomenclature

Symbols

C_p	Specific heat capacity	J kg⁻¹K⁻¹
$\bar{C}_p$	Integrated specific heat capacity	J kg⁻¹K⁻¹
FS	Full scale	–
D	Diameter	m
G	Mass flux	kg m⁻²s⁻¹
g	Acceleration due to gravity	m s⁻²
Gr	Grashof number	–
h	Specific enthalpy	J kg⁻¹
ID	Internal diameter	m
k	Thermal conductivity	W m⁻¹K⁻¹
$MAPE$	Mean absolute percent error	%
$\dot{m}$	Mass flow rate	kg s⁻¹
Nu	Nusselt number	–
P	Pressure	MPa
Pr	Prandtl number	–
$\dot{Q}$	Heat Duty	W
q''	Heat flux	W cm⁻²
Re	Reynolds number	–
R_α	Heat transfer coefficient ratio	–
T	Temperature	°C
x	Local position, distance	m

Greek Letters

α	Convective heat transfer coefficient	W m^{-2} K^{-1}
δ	Distance in flux meter	m
μ	Dynamic viscosity	kg m^{-1} s^{-1}
ν	Kinematic viscosity	m^2 s^{-1}
ρ	Density	kg m^{-3}
ψ	Acceleration parameter	

Subscripts

A, B	Flux meter location	
ADC	Analog-to-digital	
ave	Average	
b	Bulk	
$b - IG$	Bulk evaluated ideal gas property	
$chan$	Channel	J kg^{-1}K^{-1}
$corr$	Correlation	
ex	exit	
$film$	Film temperature	
$fluid$	Fluid	
FM	Flux meter	
H	Hydraulic	
in	Inlet	
$Jack$	[41] Nusselt number	
$prec$	Precision	
PC	Pseudo-critical	
Q	Thermal energy	
q	Grashof number based on heat flux	
R	Reduced	

sCO_2 Supercritical carbon dioxide

th Threshold

tot Total

UTC Uncertainty total conversion

w Wall

exp Experimental